# Observation of Topological Transition in Floquet Non-Hermitian Skin Effects in Silicon Photonics

Zhiyuan Lin,[1] Wange Song,[1,*] Li-Wei Wang,[2] Haoran Xin,[1] Jiacheng Sun,[1] Shengjie Wu,[1] Chunyu Huang,[1] Shining Zhu,[1] Jian-Hua Jiang,[3,4,2,†] and Tao Li[1,‡]

[1]*National Laboratory of Solid State Microstructures, Key Laboratory of Intelligent Optical Sensing and Manipulations, Jiangsu Key Laboratory of Artificial Functional Materials, School of Physics, College of Engineering and Applied Sciences, Nanjing University, Nanjing 210093, China*

[2]*School of Physical Science and Technology & Collaborative Innovation Center of Suzhou Nano Science and Technology, Soochow University, 1 Shizi Street, Suzhou 215006, China*

[3]*School of Biomedical Engineering, Suzhou Institute for Advanced Research, University of Science and Technology of China, Suzhou 215123, China*

[4]*School of Physics, University of Science and Technology of China, Hefei 230026, China*

(Received 14 February 2024; revised 24 May 2024; accepted 16 July 2024; published 15 August 2024)

Non-Hermitian physics has greatly enriched our understanding of nonequilibrium phenomena and uncovered novel effects such as the non-Hermitian skin effect (NHSE) that has profoundly revolutionized the field. NHSE has been predicted in systems with nonreciprocal couplings which, however, are challenging to realize in experiments. Without nonreciprocal couplings, the NHSE can also emerge in systems with coexisting gauge fields and loss or gain (e.g., in Floquet non-Hermitian systems). However, such Floquet NHSE remains largely unexplored in experiments. Here, we realize the Floquet NHSEs in periodically modulated optical waveguides integrated on a silicon photonic platform. By engineering the artificial gauge fields induced by the periodical modulation, we observe various Floquet NHSE phases and unveil their rich topological transitions. Remarkably, we discover the transitions between the unipolar NHSE phases and an unconventional bipolar NHSE phase, which is accompanied by the directional reversal of the NHSEs. The underlying physics is revealed by the band winding in complex quasienergy space which undergoes a topology change from isolated loops with the same winding to linked loops with opposite windings. Our work unfolds a new route toward Floquet NHSEs originating from the interplay between gauge fields and dissipation effects, and thus offers fundamentally new ways for steering light and other waves.

DOI: 10.1103/PhysRevLett.133.073803

Most systems and materials contain dissipation effects. In situations where the underlying physics can be described by a Hamiltonian, the Hamiltonian will become non-Hermitian with dissipation effects. The study of non-Hermitian Hamiltonians has led to the discovery of many intriguing effects, such as exceptional points [1–6] and nonorthogonal eigenstates [7]. In lattice systems, one particularly interesting phenomenon is the NHSE where an extensive number of eigenstates are localized at the boundary due to non-Hermitian effects. A direct consequence of NHSE is the breakdown of the fundamental notion of the Brillouin zone. The generalized Brillouin zone (GBZ) [8–10] is then proposed to capture the properties of finite non-Hermitian systems. Moreover, NHSEs profoundly change the topological bulk-boundary correspondence, leading to rich non-Hermitian topological physics [8,11–28].

NHSE can also be regarded as a topological effect, of which the topological invariant is the winding number of the complex energy band during its evolution in the Brillouin zone. While a unipolar NHSE is manifested in such band winding as a single loop with a finite winding number, a bipolar NHSE exhibits two linked loops with opposite winding numbers, giving rise to distinctive features such as bipolar skin localization and Bloch points [17,29–31]. In the literature, NHSEs are often based on nonreciprocal couplings which, however, are challenging in experiments and available only in a few systems [18–24,30]. In periodically driven systems (i.e., Floquet systems), the artificial gauge fields induced by the periodic driving play pivotal roles in both NHSEs and topological phenomena [32–49], leading to intriguing effects at the interface between non-Hermitian and topological physics such as the hybrid skin-topological effects [32,33]. Notably, in Floquet systems, NHSEs can be triggered solely by the on-site loss or gain [32,45–49] without relying on nonreciprocal couplings, which thus makes NHSEs more accessible. Furthermore,

*Contact author: songwange@nju.edu.cn
†Contact author: jhjiang3@ustc.edu.cn
‡Contact author: taoli@nju.edu.cn

 

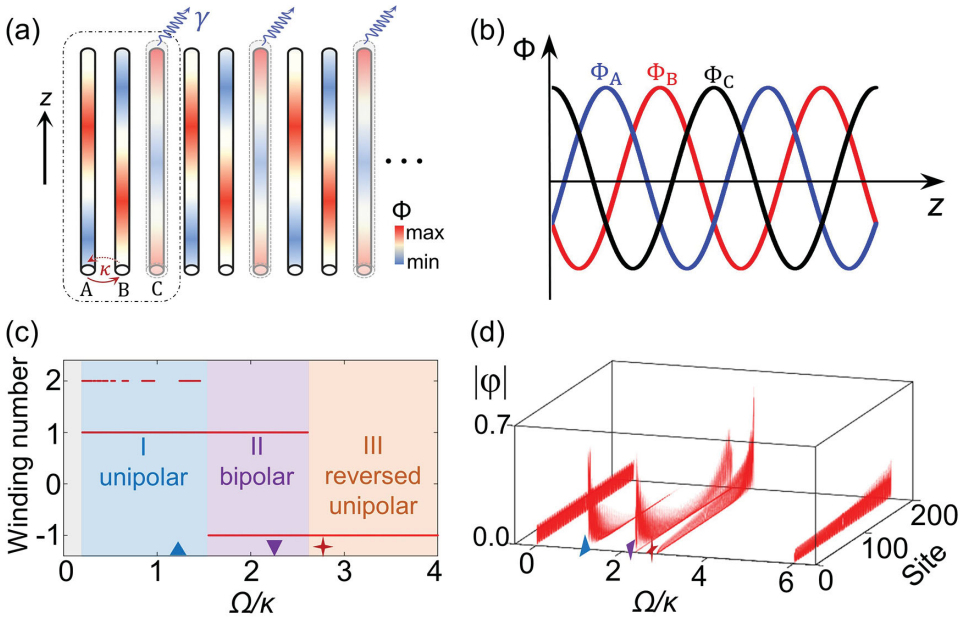


FIG. 1. Floquet NHSE: its realization and topological transition. (a) The schematic of the artificial gauge potentials induced by modulating the width of the waveguides. A unit cell (marked by the dotted box) has three sites (labeled A, B, and C). Here $\kappa$ is the coupling coefficient. A and B are lossless and C is lossy. (b) The illustration of the gauge potentials on the three waveguides versus the coordinate $z$. (c) Winding numbers of band set I as a function of modulation frequency, showing the transition between three Floquet NHSE phases, i.e., the unipolar, bipolar, and reversed unipolar NHSEs (labeled as blue, purple, and orange, separately). (d) Eigenstate profiles for different modulation frequencies. From left to right, $\Omega/\kappa = 0.0$, 1.2, 2.3, 2.8, and 6.0. The upper triangle, down triangle, and the star label the cases of the unipolar, bipolar, and the reversed unipolar NHSEs, respectively.

Floquet non-Hermitian systems are highly tunable and versatile, and have been utilized for the discovery of topological lasers [50] and other interesting effects [51–53].

Despite that considerable efforts have been made, the experimental realization of Floquet NHSE and its dynamics in integrated silicon photonics remains a big challenge due to the difficulties in simultaneous accurate control of the non-Hermitian effects and the Floquet modulation in genuine optical systems. Here, we propose an efficient approach to realize such Floquet NHSEs of light through engineering the interplay between the artificial gauge fields and the loss in the coupled optical waveguides on a silicon substrate. Via this approach, we realize and observe experimentally various Floquet NHSEs as well as their rich transitions. We discover a unipolar-bipolar transition in the NHSE by tuning the modulation periodicity and the dissipation (via chromium doping) [54]. Interestingly, the bipolar Floquet NHSE phase serves as the passage for the transition between the two unipolar Floquet NHSEs with opposite skin directions. In the complex quasienergy plane, these transitions are manifested as the change of the topology in the band winding: transforming between the isolated loops with finite winding numbers in the unipolar Floquet NHSEs and the linked loops with opposite winding numbers in the bipolar Floquet NHSE.

We start with a one-dimensional lattice of coupled optical waveguides with $N$ unit cells, as shown in Fig. 1(a). Each unit cell (marked by the dot-dashed box) contains three sublattice sites (waveguides) labeled A, B, and C, respectively. The on-site potential (propagation constant) of sublattice site $\xi(\xi \in \{\mathrm{A}, \mathrm{B}, \mathrm{C}\})$ in the $n$th unit cell is $V_{n,\xi}$ and the nearest-neighbor coupling is $\kappa$. There is an inhomogeneous dissipation distribution in each unit cell. We choose $V_{n,\xi} = \Phi_{n,\xi}$ for sites $A$ and $B$, while the site $C$ is lossy and $V_{n,C} = \Phi_{n,C} + i\gamma$, where $\Phi_{n,\xi}$ is real part of propagation constant ($z$-dependent) in each waveguide [denoted as $\Phi_{\mathrm{A}}$, $\Phi_{\mathrm{B}}$, and $\Phi_{\mathrm{C}}$ for different sublattice sites, see Fig. 1(b)]. In the tight-binding approximation, the $z$-dependent Hamiltonian of the model can be written as

$$\begin{aligned} H(z) = & \sum_{n=1}^{N} [\kappa |n, \mathrm{A}\rangle\langle n, \mathrm{B}| + \kappa |n, \mathrm{B}\rangle\langle n, \mathrm{C}| + \mathrm{H.c.}] \\ & + \sum_{n=1}^{N-1} [\kappa |n, \mathrm{C}\rangle\langle n+1, \mathrm{A}| + \mathrm{H.c.}] \\ & + \sum_{n=1}^{N} \sum_{\xi \in \{\mathrm{A},\mathrm{B},\mathrm{C}\}} \Phi_{n,\xi}(z) |n, \xi\rangle\langle n, \xi| \\ & + \sum_{n=1}^{N} i\gamma |n, \mathrm{C}\rangle\langle n, \mathrm{C}|, \end{aligned} \tag{1}$$

where Dirac's notation has been used for convenience. For instance, $|n, \xi\rangle$ denotes the state on the site $\xi$ in the $n$th unit cell. Here, we consider a sinusoidal modulation

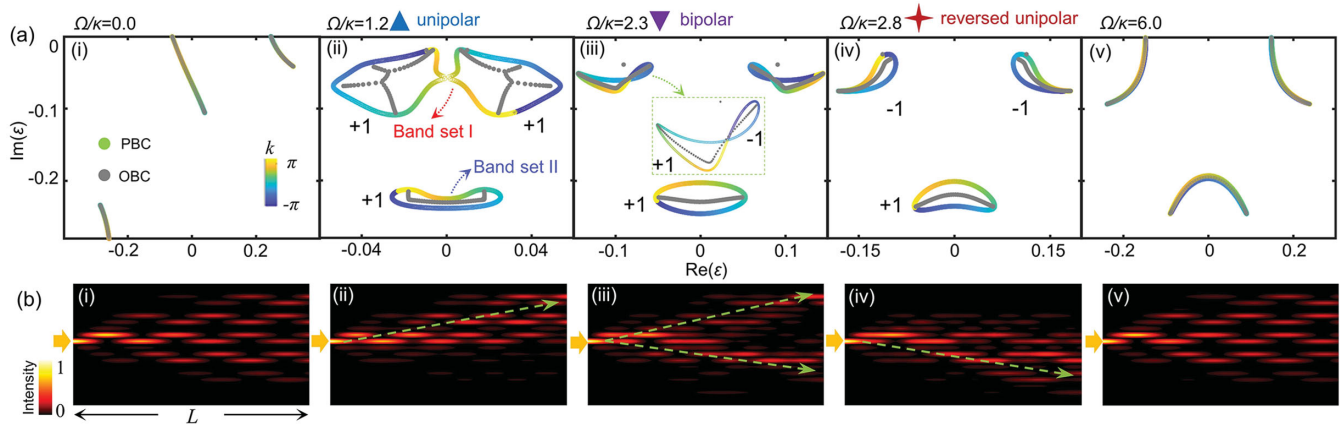


FIG. 2. Quasienergy spectrum, winding numbers, and light propagation. (a) Quasienergy spectrum under OBC and PBC for different modulation frequencies $\Omega/\kappa = 0.0$ (i), 1.2 (ii), 2.3 (iii), 2.8 (iv), and 6.0 (v). Multiple skin mode topological transitions occur as modulation frequency increases, from unipolar (ii) to bipolar (iii) and then to reversed unipolar (iv). (b) Light propagation dynamics in optical waveguide lattices with 16 sites for $\Omega/\kappa = 0.0$ (i), 1.2 (ii), 2.3 (iii), 2.8 (iv), and 6.0 (v). The intensity is normalized to 1 at every $z$ for clearer presentation. Here $\mathcal{V}/\kappa = 1.2$, $\gamma/\kappa = 2.2$, and $L = 2L_0$, where $L_0 = 2\pi/(1.2\kappa)$.

$\Phi_m(z) = \mathcal{V}\cos(\Omega z + \rho_m)$ with the initial phase $\rho_m = 2m\pi/3$, where $\mathcal{V}$ is the amplitude, $\Omega = 2\pi/p$ is the modulation frequency, and $p$ is the modulation period along the $z$ direction. This modulation is realized by engineering the $z$-dependent propagation constant in each waveguide which directly determines the phase of photons propagating in the waveguide. The $z$-dependent propagation constant can be viewed as the "gauge potential," see Supplemental Material S1 [55] for more details.

In periodically modulated systems, the effective $z$-independent Hamiltonian $H_F$ is given by Floquet theory [56,60,61] (see details in the Supplemental Material S2 [55]), which dictates the complex quasienergy $\varepsilon$ in our non-Hermitian systems [10,15,16,27]. $H_F$ can often be written in terms of a perturbative expansion in powers of $1/\Omega$, which coincides with the physical intuition that faster driving leads to weaker effects. We can thus use the modulation frequency $\Omega$ to tune the NHSE. Indeed, by tuning $\Omega$, we can substantially change the Hamiltonian $H_F$ and the NHSE. As shown in Figs. 1(c) and 1(d), the NHSE exhibits rich transitions when the modulation frequency $\Omega$ is tuned. The unipolar-dipolar transitions of NHSE in Fig. 1(d) are the topological transitions characterized by the change of the winding number of the quasienergy bands, as revealed below.

The topology of the NHSE can be characterized by the winding number of each quasienergy band derived from $H_F$ in the complex energy plane under the periodic boundary condition (PBC) [57,58]

$$\mathcal{W}(E) = \frac{1}{2\pi i}\oint_{\mathrm{BZ}} \partial_k \ln\det[H_F(k) - E]dk. \qquad (2)$$

The loop formed by the quasienergy spectrum in the complex energy plane as the wave vector $k$ traverses the Brillouin zone, is one of the hallmarks of NHSE and has nontrivial topological properties [17,26,28,30]. The winding number $\mathcal{W}$ is a topological invariant for any energy $E$ within the loop. This winding number characterizes the direction of the exponential decay of the eigenstate wave functions and thus determines the direction of the NHSE.

In our system, the spectrum and the winding number for each of the three quasienergy bands change with the modulation frequency $\Omega$. For $\Omega/\kappa = 0$, the spectrum does not form any loop and there is no NHSE [Fig. 2(a)(i)]. At $\Omega/\kappa = 1.2$, the spectrum has three loops which all have the winding number of 1 [Fig. 2(a)(ii)], yielding the NHSE toward the left boundary, which is the signature of the unipolar phase I ($0.2 < \Omega/\kappa < 1.54$) (Here, the left and right directions are defined in the view of the forward-going photons). At $\Omega/\kappa = 2.3$, two of the three loops become twisted loops, signifying a topological transition, whereas the third loop's topology remains the same [Fig. 2(a)(iii)]. Each twisted loop consists of two parts with opposite winding numbers. This corresponds to the region $1.54 < \Omega/\kappa < 2.6$, which gives the bipolar phase II. In this phase, the NHSE becomes bipolar, i.e., about half of the eigenstates have wave functions localized toward the left boundary, while the other half of the eigenstates are localized toward the right boundary. At $\Omega/\kappa = 2.8$, the two twisted loops become simple loops, but the winding number is switched to $-1$. Thus, this phase (i.e., phase III in the region $\Omega/\kappa > 2.6$) corresponds to the unipolar NHSE towards the right boundary (denoted as the reversed unipolar phase). In the above process, the unipolar NHSE switches direction through the bipolar NHSE, yielding rich topological transitions (see the exact variation of the complex bands with modulation frequency in Supplemental Material, video 1 [55]).

It should be noted that the three loops correspond to the three energy bands. As two of these bands may overlap

with each other, we denote them as band set I, while the remaining band set is denoted as band set II [see Fig. 2(a)(ii)]. The topology transition studied here takes place in band set I which is symmetric with respect to $\mathrm{Re}(\varepsilon) = 0$ (The band set II also has topological transitions but not in the same region; see exact variation of the complex bands in Supplemental Material, video 1 [55]). As the two loops in band set I have the same winding number, we shall focus only on the loop which is mainly in the region $\mathrm{Re}(\varepsilon) < 0$. The winding number of such a loop is presented in Fig. 1(c).

Several remarks are in order. First, the strength of the NHSE is determined by the area of the loop [17]. For instance, at very large $\Omega/\kappa$, although the two loops of band set I have winding number $\mathcal{W} = -1$, the areas of the loops are very small, therefore the NHSE is very weak [see Fig. 1(d) for the eigenstates wave functions at $\Omega/\kappa = 6.0$]. Second, one may notice in Fig. 1(c) that at some $\Omega/\kappa$, there are two winding numbers: $\mathcal{W} = 2$ and 1. This is because the evolution of the loops is much more complicated than illustrated in Fig. 2 (see such evolution in Supplemental Material, video 1 [55]). The winding numbers are calculated for all open-boundary-condition (OBC) eigenenergies enclosed by the loops. Therefore, there can be multiple values of the winding numbers for each set of parameters. Nevertheless, both winding numbers 2 and 1 give rise to the same NHSE towards the left boundary, which is consistent with the calculated wave functions. Finally, the winding numbers at $\Omega/\kappa < 0.2$ are not studied in this work because in this regime the quasienergy bands can be scrambled and the winding numbers can be noninteger. In this region, the calculated eigenstate wave functions indicate that the system has no noticeable NHSE [e.g., see Figs. 1(d) and 2(b)(i)].

To confirm the above phenomena, we demonstrate the dynamics of the light field in the coupled optical waveguide arrays along the $z$ direction. The initial excitation is via site $B$ at the center of the waveguide array. Such excitation is chosen because site $B$ has substantial overlap with the eigenstates of band set I. Consequently, the light dynamics predominantly capture the properties of the eigenmodes of band set I. It should be mentioned that initial excitation at the lossy waveguide C excites mainly the eigenmodes of band set II, which is not considered here. The light propagation dynamics in the optical waveguide system are simulated using coupled-mode theory. As shown in Fig. 2(b)(i), the dynamics at $\Omega/\kappa = 0.0$ is consistent with the conventional quantum walk on a discrete lattice, showing no feature of NHSE but instead with a broadened peak at the center of the system. At $\Omega/\kappa = 1.2$ [see Fig. 2(b)(ii)], as indicated by the dashed arrow, the NHSE toward the left boundary is notable. At $\Omega/\kappa = 2.3$, as shown in Fig. 2(b)(iii), there are salient features of the bipolar NHSE. In particular, when compared with the case with $\Omega/\kappa = 0.0$, the light wave amplitude at the system center is suppressed, which indicates the bipolar NHSE. At $\Omega/\kappa = 2.8$, the light propagation dynamics in Fig. 2(b)(iv) shows clear features of the NHSE toward the right boundary, indicating the reversal of the direction of the NHSE. At significantly large $\Omega/\kappa$ (e.g., $\Omega/\kappa = 6.0$), the NHSE is effectively suppressed, and the wave dynamics are similar to that in Fig. 2(b)(v). The wave dynamics for other $\Omega/\kappa$ are also shown in Supplemental Material, video 2 [55]. These simulation results are consistent with the prediction from the eigenspectrum and the winding numbers, indicating that these effects can possibly be observed in optical experiments.

To observe the predicted NHSEs in silicon photonics, we consider an optical lattice comprised of 16 Si waveguides on the sapphire substrate with air cladding [Fig. 3(a)]. The waveguide height is $h = 220$ nm and the waveguide spacing is $g = 150$ nm. The waveguide width is periodically modulated in a sinusoidal way with averaged width $w = 400$ nm and the modulation amplitude $\Delta w = 20$ nm. The modulation period $p$ is tuned [$p = \infty$ (static), 43, 21, 15, and 8 μm] to achieve different NHSE phases. The loss is introduced by coating a layer of chromium (Cr) with width $w_c = 200$ nm and thickness $h_c = 8$ nm on top of every three Si waveguides [55]. The scanning electron microscope (SEM) pictures of experimentally fabricated samples are shown in Fig. 3(b), where the width modulations and deposited Cr can be clearly observed from the enlarged picture at the bottom panel.

In experiments, we fabricated five types of samples, each with distinct modulation periods, i.e., $p = \infty$ (no modulation), 43, 21, 15, and 8 μm, corresponding to five different cases of non-Hermitian dynamics shown in Fig. 1. To capture various stages of mode evolutions, we fabricated a set of 4 samples with different propagation lengths ($L/4$, $L/2$, $3L/4$, and $L$) for each case. For each sample, a near-infrared laser (1550 nm wavelength) is incident into site $B$ at the center of the waveguide lattices from a grating coupler, and the output intensity distribution was measured by a near-infrared camera through a microscope objective. The experimental results are presented in Fig. 3(c), along with simulated light evolutions (using the commercial finite-element software COMSOL Multiphysics5.6) for further verification (see the extracted data in Supplemental Material S3 [55]). When the system is static ($p = \infty$ μm), the light evolution is broadened, as shown in Fig. 3(c)(i). At the appropriate modulation period ($p = 43$ μm), light excited from the central waveguide gradually evolves towards one end of the boundary, which is typical of the unipolar skin effect, as shown in Fig. 3(c)(ii). The experimentally captured output results for different propagation lengths demonstrate a gradual unidirectional evolution of the light field towards one end of the boundary with increasing propagation length, aligning closely with the simulation results. By further decreasing the modulation period, e.g., when $p = 21$ μm, light

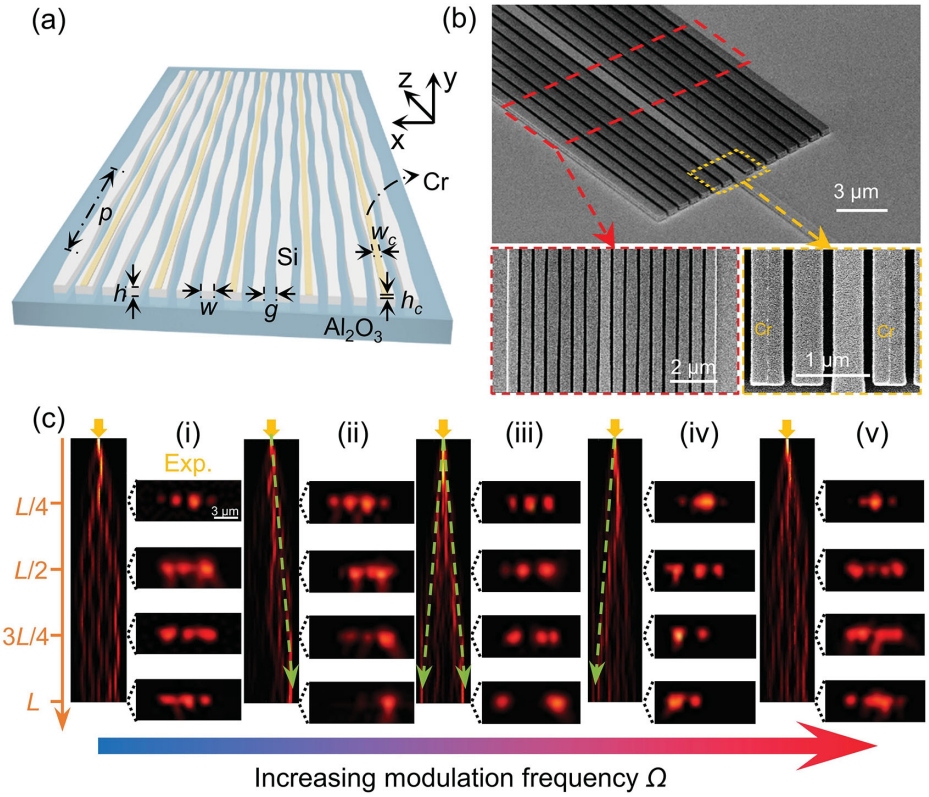


FIG. 3. Realizing Floquet NHSEs in on-chip silicon waveguides. (a) Schematic of the silicon waveguide design. The waveguide width is varied along the propagation direction and Cr is deposited on top of every three silicon waveguides (labeled by yellow). (b) SEM image of one of the experimentally fabricated samples. The bottom panels show enlarged views. The waveguide width modulation and Cr strips can be clearly observed (the horizontal-to-vertical scale ratio is 4:1 for clearer presentation). (c) Simulation results for light propagation along the $z$ direction (left) and the experimentally measured light intensities (right) at different propagation lengths ($L/4$, $L/2$, $3L/4$, and $L$, with $L = 86$ μm). The modulation periods are (i) $p = \infty$ (no modulation), (ii) $p = 43$, (iii) $p = 21$, (iv) $p = 15$, and (v) $p = 8$ μm. The intensity is normalized to 1 at every $z$ in the simulation results.

excited from the central waveguide eventually evolves towards both ends [Fig. 3(c)(iii)], which is the characteristic of bipolar NHSE. This feature is clearly captured by the experiments, showcasing the light's ultimate tendency to both ends of the boundary, indicating the skin mode transitions. Notably, when $p = 15$ μm in Fig. 3(c)(iv), a reversed skin effect becomes evident. The experimental output with different propagation lengths demonstrated consistent results, i.e., the final output spot is at the opposite boundary compared with the NHSE shown in Fig. 3(c)(ii). When the modulation period is much smaller [$p = 8$ μm in Fig. 3(c)(v)], the NHSEs become challenging to discern due to the fact that the quasienergy spectra at the PBC and OBC are nearly the same. In this case, the Floquet NHSE is unnoticeable in both experiments and simulations.

The underlying physics of the observed Floquet NHSEs becomes clearer in the Floquet-Hilbert space [60,62,63] (see Supplemental Material S2 [55]) by mapping the 1D $z$-dependent model into a 2D $z$-independent problem. It is found that nonzero effective magnetic flux will arise in the synthetic static lattice that interacts with loss, and giving rise to nonvanishing currents through the system due to nonzero area of loops in the PBC spectra (Fig. 2), which is the origin of the Floquet NHSEs [17,26]. When the modulation frequency is increasing, interactions between magnetic flux and loss become complex, resulting in creation of multiple currents with different directions. The generation and annihilation of these nonvanishing currents during the interactions give rise to topological transitions. It is noteworthy that using our design strategy and the controllable Floquet NHSE, an on-chip *Floquet topological funneling* of light [18] can also be achieved. Such a funnel can steer any light field injected into the structure (irrespective of its shape and input position) toward the system center via the Floquet NHSEs [55].

In summary, we demonstrate the Floquet NHSEs with topological transitions in periodically modulated coupled waveguides on a silicon photonics platform at telecommunication frequencies. By engineering the interplay between the artificial gauge fields induced by the periodic modulation and the optical loss in the waveguides, we observe various Floquet NHSEs and discover their rich transitions. These transitions are manifested as the topological transitions in the band winding in complex quasienergy space.

For instance, the transition from a unipolar Floquet NHSE state to a bipolar Floquet NHSE state is accompanied with a transition from a single loop with finite winding number to two linked loops with opposite winding numbers in the complex quasi-energy space. We characterize these Floquet NHSEs via optical measurements and show that they can also be used to realize topological funneling of light via engineering the Floquet NHSE states. These findings unveil a regime where the interplay between gauge fields and dissipation yields fruitful physics and provides new principles for manipulating light and other waves, inspiring future research on exploring various non-Hermitian phenomena such as wave self-healing [13] and self-acceleration [59] in the same silicon photonics platform.

*Acknowledgments*—The authors acknowledge the financial support from The National Key R&D Program of China (No. 2023YFA1407700), National Natural Science Foundation of China (Nos. 12174186, 12204233, 62288101, 92250304, 62325504, and 12125504). Jian-Hua Jiang thanks the support from the CAS Pioneer Hundred Talents Program and the Gusu Leading Innovation Scientists Program of Suzhou City. Tao Li thanks the support from Dengfeng Project B of Nanjing University.

[1] W. J. Chen, S. K. Özdemir, G. M. Zhao, J. Wiersig, and L. Yang, Exceptional points enhance sensing in an optical microcavity, Nature (London) **548**, 192 (2017).
[2] J. Doppler, A. A. Mailybaev, J. Böhm, U. Kuhl, A. Girschik, F. Libisch, T. J. Milburn, P. Rabl, N. Moiseyev, and S. Rotter, Dynamically encircling an exceptional point for asymmetric mode switching, Nature (London) **537**, 76 (2016).
[3] H. Hodaei, A. U. Hassan, S. Wittek, H. Garcia-Gracia, R. El-Ganainy, D. N. Christodoulides, and M. Khajavikhan, Enhanced sensitivity at higher-order exceptional points, Nature (London) **548**, 187 (2017).
[4] M.-A. Miri and A. Alù, Exceptional points in optics and photonics, Science **363**, eaar7709 (2019).
[5] X. L. Zhang, T. S. Jiang, and C. T. Chan, Dynamically encircling an exceptional point in anti-parity-time symmetric systems: Asymmetric mode switching for symmetry-broken modes, Light Sci. Appl. **8**, 88 (2019).
[6] A. D. Li, H. Wei, M. Cotrufo, W. J. Chen, S. Mann, X. Ni, B. C. Xu, J. F. Chen, J. Wang, S. H. Fan, C. W. Qiu, A. Alú, and L. Chen, Exceptional points and non-Hermitian photonics at the nanoscale, Nat. Nanotechnol. **18**, 706 (2023).
[7] C. E. Rüter, K. G. Makris, R. El-Ganainy, D. N. Christodoulides, M. Segev, and D. Kip, Observation of parity-time symmetry in optics, Nat. Phys. **6**, 192 (2010).
[8] F. Song, S. Y. Yao, and Z. Wang, Non-Hermitian skin effect and chiral damping in open quantum systems, Phys. Rev. Lett. **123**, 170401 (2019).
[9] Z. Yang, K. Zhang, C. Fang, and J. Hu, Non-Hermitian bulk-boundary correspondence and auxiliary generalized brillouin zone theory, Phys. Rev. Lett. **125**, 226402 (2020).
[10] S. Y. Yao and Z. Wang, Edge states and topological invariants of non-Hermitian systems, Phys. Rev. Lett. **121**, 086803 (2018).
[11] D. S. Borgnia, A. J. Kruchkov, and R. J. Slager, Non-Hermitian boundary modes and topology, Phys. Rev. Lett. **124**, 056802 (2020).
[12] S. Longhi, Non-Bloch-band collapse and chiral Zener tunneling, Phys. Rev. Lett. **124**, 066602 (2020).
[13] S. Longhi, Self-healing of non-Hermitian topological skin modes, Phys. Rev. Lett. **128**, 157601 (2022).
[14] W.-T. Xue, Y.-M. Hu, F. Song, and Z. Wang, Non-Hermitian edge burst, Phys. Rev. Lett. **128**, 120401 (2022).
[15] Y. Yi and Z. Yang, Non-Hermitian skin modes induced by on-site dissipations and chiral tunneling effect, Phys. Rev. Lett. **125**, 186802 (2020).
[16] K. Yokomizo and S. Murakami, Non-Bloch band theory of non-Hermitian systems, Phys. Rev. Lett. **123**, 066404 (2019).
[17] K. Zhang, Z. S. Yang, and C. Fang, Correspondence between winding numbers and skin modes in non-Hermitian systems, Phys. Rev. Lett. **125**, 126402 (2020).
[18] S. Weidemann, M. Kremer, T. Helbig, T. Hofmann, A. Stegmaier, M. Greiter, R. Thomale, and A. Szameit, Topological funneling of light, Science **368**, 311 (2020).
[19] L. Zhang, Y. H. Yang, Y. Ge, Y. J. Guan, Q. L. Chen, Q. H. Yan, F. J. Chen, R. Xi, Y. Z. Li, D. Jia, S. Q. Yuan, H. X. Sun, H. S. Chen, and B. L. Zhang, Acoustic non-Hermitian skin effect from twisted winding topology, Nat. Commun. **12**, 6297 (2021).
[20] Q. Lin, W. Yi, and P. Xue, Manipulating directional flow in a two-dimensional photonic quantum walk under a synthetic magnetic field, Nat. Commun. **14**, 6283 (2023).
[21] Q. Zhou, J. Wu, Z. Pu, J. Lu, X. Huang, W. Deng, M. Ke, and Z. Liu, Observation of geometry-dependent skin effect in non-Hermitian phononic crystals with exceptional points, Nat. Commun. **14**, 4569 (2023).
[22] D. Y. Zou, T. Chen, W. J. He, J. C. Bao, C. H. Lee, H. J. Sun, and X. D. Zhang, Observation of hybrid higher-order skin-topological effect in non-Hermitian topolectrical circuits, Nat. Commun. **12**, 7201 (2021).
[23] L. Xiao, T. S. Deng, K. K. Wang, G. Y. Zhu, Z. Wang, W. Yi, and P. Xue, Non-Hermitian bulk-boundary correspondence in quantum dynamics, Nat. Phys. **16**, 761 (2020).
[24] W. Wang, X. L. Wang, and G. C. Ma, Non-Hermitian morphing of topological modes, Nature (London) **608**, 50 (2022).
[25] L. Li, C. H. Lee, S. Mu, and J. Gong, Critical non-Hermitian skin effect, Nat. Commun. **11**, 5491 (2020).
[26] K. Zhang, Z. S. Yang, and C. Fang, Universal non-Hermitian skin effect in two and higher dimensions, Nat. Commun. **13**, 2496 (2022).
[27] R. J. Lin, T. M. Y. Tai, L. H. Li, and C. H. Lee, Topological non-Hermitian skin effect, Front. Phys. **18**, 53605 (2023).
[28] H. Hu and E. Zhao, Knots and non-Hermitian Bloch bands, Phys. Rev. Lett. **126**, 010401 (2021).
[29] W. T. Xue, M. R. Li, Y. M. Hu, F. Song, and Z. Wang, Simple formulas of directional amplification from non-Bloch band theory, Phys. Rev. B **103**, L241408 (2021).

[30] K. Wang, A. Dutt, K. Y. Yang, C. C. Wojcik, J. Vuckovic, and S. H. Fan, Generating arbitrary topological windings of a non-Hermitian band, Science **371**, 1240 (2021).
[31] N. Okuma, K. Kawabata, K. Shiozaki, and M. Sato, Topological origin of non-Hermitian skin effects, Phys. Rev. Lett. **124**, 086801 (2020).
[32] Y. H. Li, C. Liang, C. Y. Wang, C. C. Lu, and Y. C. Liu, Gain-loss-induced hybrid skin-topological effect, Phys. Rev. Lett. **128**, 223903 (2022).
[33] W. W. Zhu and J. B. Gong, Hybrid skin-topological modes without asymmetric couplings, Phys. Rev. B **106**, 035425 (2022).
[34] L. W. Zhou, Y. J. Gu, and J. B. Gong, Dual topological characterization of non-Hermitian Floquet phases, Phys. Rev. B **103**, L041404 (2021).
[35] X. Zhang and J. Gong, Non-Hermitian Floquet topological phases: Exceptional points, coalescent edge modes, and the skin effect, Phys. Rev. B **101**, 045415 (2020).
[36] L. W. Zhou and J. B. Gong, Non-Hermitian Floquet topological phases with arbitrarily many real-quasienergy edge states, Phys. Rev. B **98**, 205417 (2018).
[37] Y. Cao, Y. Li, and X. Yang, Non-Hermitian bulk-boundary correspondence in a periodically driven system, Phys. Rev. B **103**, 075126 (2021).
[38] T. Y. Li, Y. S. Zhang, and W. Yi, Two-dimensional quantum walk with non-Hermitian skin effects, Chin. Phys. Lett. **38**, 030301 (2021).
[39] C. H. Lee and S. Longhi, Ultrafast and anharmonic Rabi oscillations between non-Bloch bands, Commun. Phys. **3**, 147 (2020).
[40] H. Wu and J.-H. An, Floquet topological phases of non-Hermitian systems, Phys. Rev. B **102**, 041119(R) (2020).
[41] H. Gao, H. R. Xue, Z. M. Gu, L. H. Li, W. W. Zhu, Z. Q. Su, J. Zhu, B. L. Zhang, and Y. D. Chong, Anomalous Floquet non-Hermitian skin effect in a ring resonator lattice, Phys. Rev. B **106**, 134112 (2022).
[42] L. W. Zhou, R. W. Bomantara, and S. L. Wu, qth-root non-Hermitian Floquet topological insulators, SciPost Phys. **13**, 015 (2022).
[43] H. Liu and I. C. Fulga, Mixed higher-order topology: Boundary non-Hermitian skin effect induced by a Floquet bulk, Phys. Rev. B **108**, 035107 (2023).
[44] C.-H. Liu, H. Hu, S. Chen, and X.-J. Liu, Anomalous second-order skin modes in Floquet non-Hermitian systems, Phys. Rev. B **108**, 174307 (2023).
[45] Y. Sun, X. Hou, T. Wan, F. Wang, S. Zhu, Z. Ruan, and Z. Yang, Photonic Floquet skin-topological effect, Phys. Rev. Lett. **132**, 063804 (2024).
[46] C. Shu, K. Zhang, and K. Sun, Loss-induced universal one-way transport in periodically driven systems, Phys. Rev. B **109**, 184302 (2024).
[47] Y. Li, C. Lu, S. Zhang, and Y.-C. Liu, Loss-induced Floquet non-Hermitian skin effect, Phys. Rev. B **108**, L220301 (2023).
[48] S. L. Ke, W. T. Wen, D. Zhao, and Y. Wang, Floquet engineering of the non-Hermitian skin effect in photonic waveguide arrays, Phys. Rev. A **107**, 053508 (2023).
[49] C. Jiang, Y. Liu, X. H. Li, Y. L. Song, and S. L. Ke, Twist-induced non-Hermitian skin effect in optical waveguide arrays, Appl. Phys. Lett. **123**, 151101 (2023).
[50] S. K. Ivanov, Y. Q. Zhang, Y. V. Kartashov, and D. V. Skryabin, Floquet topological insulator laser, APL Photonics **4**, 126101 (2019).
[51] M. S. Rudner and N. H. Lindner, Band structure engineering and non-equilibrium dynamics in Floquet topological insulators, Nat. Rev. Phys. **2**, 229 (2020).
[52] L. W. Zhou and D. J. Zhang, Non-Hermitian Floquet topological matter-a review, Entropy **25**, 1401 (2023).
[53] S. Yin, E. Galiffi, and A. Alù, Floquet metamaterials, eLight **2**, 8 (2022).
[54] S. J. Wu, W. G. Song, S. L. Gao, Y. X. Chen, S. N. Zhu, and T. Li, Floquet pi mode engineering in non-Hermitian waveguide lattices, Phys. Rev. Res. **3**, 023211 (2021).
[55] See Supplemental Material at http://link.aps.org/supplemental/10.1103/PhysRevLett.133.073803 which includes Refs. [56,60–63], for additional information about the detailed derivations of artificial gauge transformation, the introduction of Floquet-Hilbert space, and experimental methods.
[56] T. Oka and S. Kitamura, Floquet engineering of quantum materials, Annu. Rev. Condens. Matter Phys. **10**, 387 (2019).
[57] Z. P. Gong, Y. Ashida, K. Kawabata, K. Takasan, S. Higashikawa, and M. Ueda, Topological phases of non-Hermitian systems, Phys. Rev. X **8**, 031079 (2018).
[58] K. Kawabata, K. Shiozaki, M. Ueda, and M. Sato, Symmetry and topology in non-Hermitian physics, Phys. Rev. X **9**, 041015 (2019).
[59] S. Longhi, Non-Hermitian skin effect and self-acceleration, Phys. Rev. B **105**, 245143 (2022).
[60] A. Eckardt and E. Anisimovas, High-frequency approximation for periodically driven quantum systems from a Floquet-space perspective, New J. Phys. **17**, 093039 (2015).
[61] M. Rodriguez-Vega, M. Vogl, and G. A. Fiete, Low-frequency and Moire-Floquet engineering: A review, Ann. Phys. (Amsterdam) **435**, 168434 (2021).
[62] M. R. Rodriguez-Vega, M. Lentz, and B. Seradjeh, Floquet perturbation theory: Formalism and application to low-frequency limit, New J. Phys. **20**, 093022 (2018).
[63] H. Sambe, Steady states and quasienergies of a quantum-mechanical system in an oscillating field, Phys. Rev. A **7**, 2203 (1973).